

Electronic Supplementary Information (ESI)

Designed Metal-Organic Framework Based on Metal-Organic Polyhedron with High Performance for Carbon Dioxide Capture and Separation of Light Hydrocarbon

Dongmei Wang, Bing Liu, Shuo Yao, Tao Wang, Guanghua Li, Qisheng Huo, and Yunling Liu*

State Key Laboratory of Inorganic Synthesis and Preparative Chemistry, College of Chemistry, Jilin University, Changchun 130012, P. R. China

Jilin University, Changchun 130012, P. R. China. E-mail: yunling@jlu.edu.cn; Fax: +86-431-85168624; Tel: +86-431-85168614

Materials and Methods

All chemicals were obtained from commercial sources and used without further purification. Powder X-ray diffraction (PXRD) data was collected on a Rigaku D/max-2550 diffractometer with Cu K α radiation ($\lambda = 1.5418 \text{ \AA}$). Elemental analyses (C, H, and N) were achieved by vario MICRO (Elementar, Germany). The thermal gravimetric analyses (TGA) were performed on TGA Q500 thermogravimetric analyzer used in air with a heating rate of $10 \text{ }^\circ\text{C min}^{-1}$.

Prediction of the Gas Adsorption Selectivity by IAST.

The measured experimental data is excess loadings (q^{ex}) of the pure components CO $_2$, CH $_4$, C $_2$ H $_6$ and C $_3$ H $_8$ for **JLU-Liu22**, which should be converted to absolute loadings (q) firstly.

$$q = q^{ex} + \frac{pV_{pore}}{ZRT}$$

Here Z is the compressibility factor. The Peng-Robinson equation was used to estimate the value of compressibility factor to obtain the absolute loading, while the measure pore volume $0.77 \text{ cm}^3 \text{ g}^{-1}$ is also necessary.

In order to perform the IAST calculations, the single-component isotherm was fitted by the

dual-site Langmuir-Freundlich (DSLFL) adsorption model to correlate the pure-component equilibrium data and further predict the adsorption of mixtures. The DSLFL model is described as:

$$q = q_{m1} \times \frac{b_1 \times p^{1/n_1}}{1 + b_1 \times p^{1/n_1}} + q_{m2} \times \frac{b_2 \times p^{1/n_2}}{1 + b_2 \times p^{1/n_2}}$$

Here p is the pressure of the bulk gas at equilibrium with the adsorbed phase (kPa), q is the adsorbed amount per mass of adsorbent (mol kg⁻¹), q_{m1} and q_{m2} are the saturation capacities of sites 1 and 2 (mol kg⁻¹), b_1 and b_2 are the affinity coefficients of sites 1 and 2 (1/kPa), n_1 and n_2 are the deviations from an ideal homogeneous surface.

To investigate the separation of binary mixtures, the adsorption selectivity is defined by

$$S_{ij} = \frac{x_1/x_2}{y_1/y_2}$$

x_1 and x_2 are the absolute component loadings of the adsorbed phase in the mixture. These component loadings are also termed the uptake capacities. We calculate the values of x_1 and x_2 using the Ideal Adsorbed Solution Theory (IAST) of Myers and Prausnitz.¹

Calculations of the Isothermic Heats of Gas Adsorption (Q_{st}):

A virial-type² expression comprising the temperature-independent parameters a_i and b_j was employed to calculate the enthalpies of adsorption for CH₄, C₂H₆ and C₃H₈ (at 273 and 298 K) on compounds. In each case, the data were fitted using the equation:

$$\ln P = \ln N + \frac{1}{T} \sum_{i=0}^m a_i N^i + \sum_{j=0}^n b_j N^j$$

Here, P is the pressure expressed in Torr, N is the amount adsorbed in mmol g⁻¹, T is the temperature in K, a_i and b_j are virial coefficients, m , n represent the number of coefficients required to adequately describe the isotherms (m and n were gradually increased until the contribution of extra added a and b coefficients was deemed to be statistically insignificant towards the overall fit, and the average value of the squared deviations from the experimental values was minimized). The values of the virial coefficients a_0 through a_m were then used to

calculate the isosteric heat of adsorption using the following expression.

$$Q_{st} = -R \sum_{i=0}^m a_i N^i$$

Q_{st} is the coverage-dependent isosteric heat of adsorption and R is the universal gas constant. The heats of gas sorption for **JLU-Liu22** in this manuscript are determined by using the sorption data measured in the pressure range from 0-1 bar (273 and 298 K for gases), which is fitted by the virial-equation very well.

Synthesis of **JLU-Liu22**

Single crystal of compound **JLU-Liu22** was obtained by solvothermal reaction of $\text{Cu}(\text{NO}_3)_2 \cdot 3\text{H}_2\text{O}$ (8 mg 0.033 mmol) and H_4tpta (2 mg, 0.005 mmol) in N,N -dimethylacetamide (DMA) (1 mL)/water (H_2O) (0.65 mL) with HNO_3 (0.65 mL) (2.2 mL HNO_3 in 10 mL DMF) at 85 °C for 24 hours and then 105 °C for 12 hours. The mixture was then cooled to room temperature. Bright-blue block crystals were obtained and air-dried (yield 60%, based on H_4tpta). Elemental analysis (%) Calcd for **JLU-Liu22** $\text{C}_{111}\text{H}_{156}\text{N}_{11}\text{O}_{50}\text{Cu}_6$: C, 45.65; H, 5.39; N, 5.72. Found: C, 46.88; H, 5.60; N, 5.42. The experimental PXRD pattern is in good agreement with the simulated one based on the single-crystal X-ray data, indicating the purity of the as-synthesized product (Fig. S5).

Single Crystal X-ray Structure Determination

Crystallographic data for **JLU-Liu22** was collected on a Bruker Apex II CCD diffractometer using graphite-monochromated Mo-K_α ($\lambda = 0.71073 \text{ \AA}$) radiation at room temperature. All non-hydrogen atoms were easily found from the difference Fourier map. The structure was solved by direct methods and refined by full-matrix least-squares on F^2 using version 5.1.³ All non-hydrogen atoms were refined anisotropically. Since the highly disordered cations and guest molecules were trapped in the channels of **JLU-Liu22** and could not be modeled properly, there are “Alert level A” about “Check Reported Molecular Weight” and “VERY LARGE Solvent Accessible VOID(S) in Structure” in the “checkCIF/PLATON report” files for **JLU-Liu22**. The final formula of **JLU-Liu22** was derived from crystallographic data combined with elemental and thermogravimetric analysis data. The detailed crystallographic data and selected bond lengths and angles for compound are listed in Table S2-S3,

respectively. Crystallographic data for **JLU-Liu22** (1410333) have been deposited with Cambridge Crystallographic Data Centre. Data can be obtained free of charge upon request at www.ccdc.cam.ac.uk/data_request/cif. Topology information for the compound was calculated by TOPOS 4.0.⁴

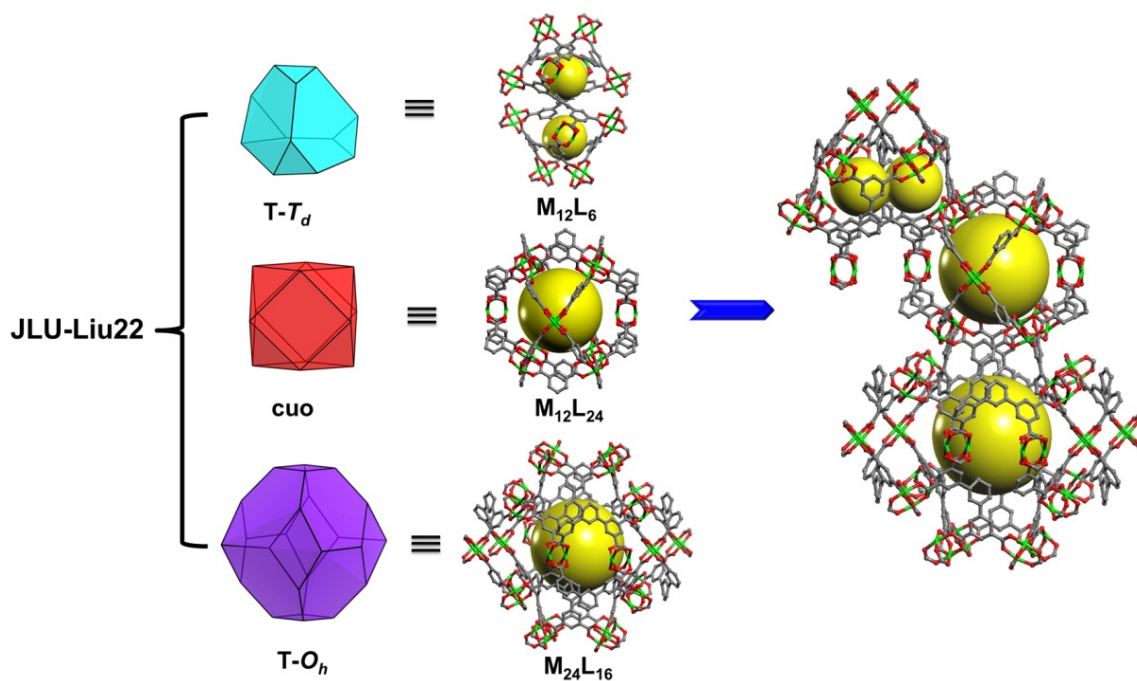


Fig. S1 Three types of different MOPs cages in the structure of **JLU-Liu22**.

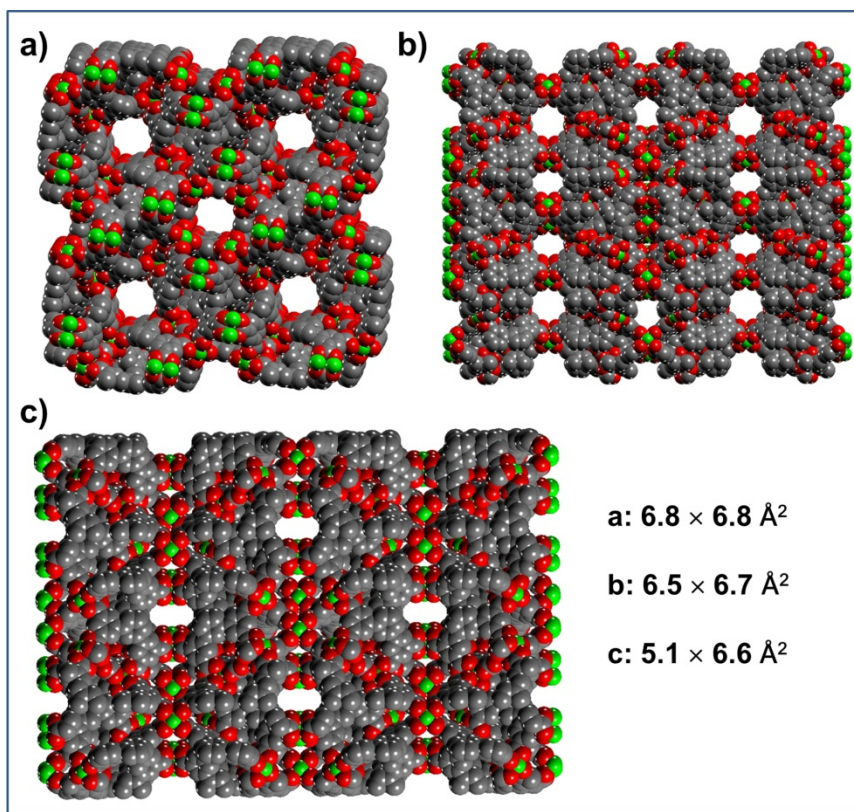


Fig. S2 CPK view of the structure of **JLU-Liu22** showing multiple pores in different directions (regardless of van der Waals radii).

Topology analysis of **JLU-Liu22**

From the viewpoints of topology, the Cu(II) paddlewheel MBBs and tpta^4 ligands both can be regarded as 4-c nodes. As a result, **JLU-Liu22** adopts a new (4,4)-connected topology with a Schläfli symbol of $\{4.6^2.8^3\}\{4.6^4.8\}\{4.6^5\}_4$. In another way, the tpta^4 ligands can be considered as two 3-c nodes, lead to a different new (3,4)-c topology with a Schläfli symbol of $\{6^2.8^2.9^2\}_2\{6^2.8\}_4\{6^2.9\}_2\{6^3.8.10^2\}$ (Fig. S3). Alternatively, the tpta^4 ligand is regarded as 2-c linker and the MOP-1 can be viewed as a SBB which gives rise to different topologies depending on the chosen vertices. Specifically, MOP-1 can be regarded as an **oct** (square-face-centers as vertices) give rise to 6-c network, and then the framework of **JLU-Liu22** belongs to **pcu** topology with a Schläfli symbol of $\{4^{12}.6^3\}$. MOP-1 can be described as a **cuo** (12 paddlewheels as vertices) leading to 12-c **fcu** topology with a Schläfli symbol of $\{3^{24}.4^{36}.5^6\}$ (Fig. S4).

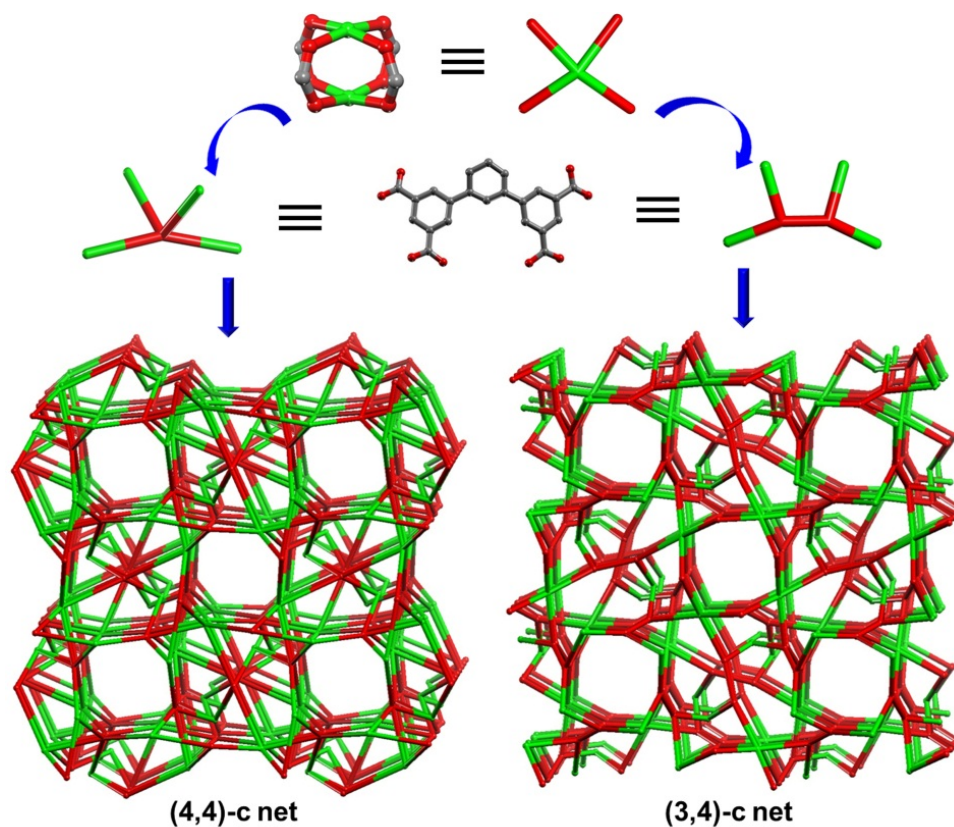


Fig. S3 The tpta⁴⁻ ligands can be regarded as 4-c node or 3-node linked by 4-c Cu paddlewheel MBBs, and then generates two different topologies.

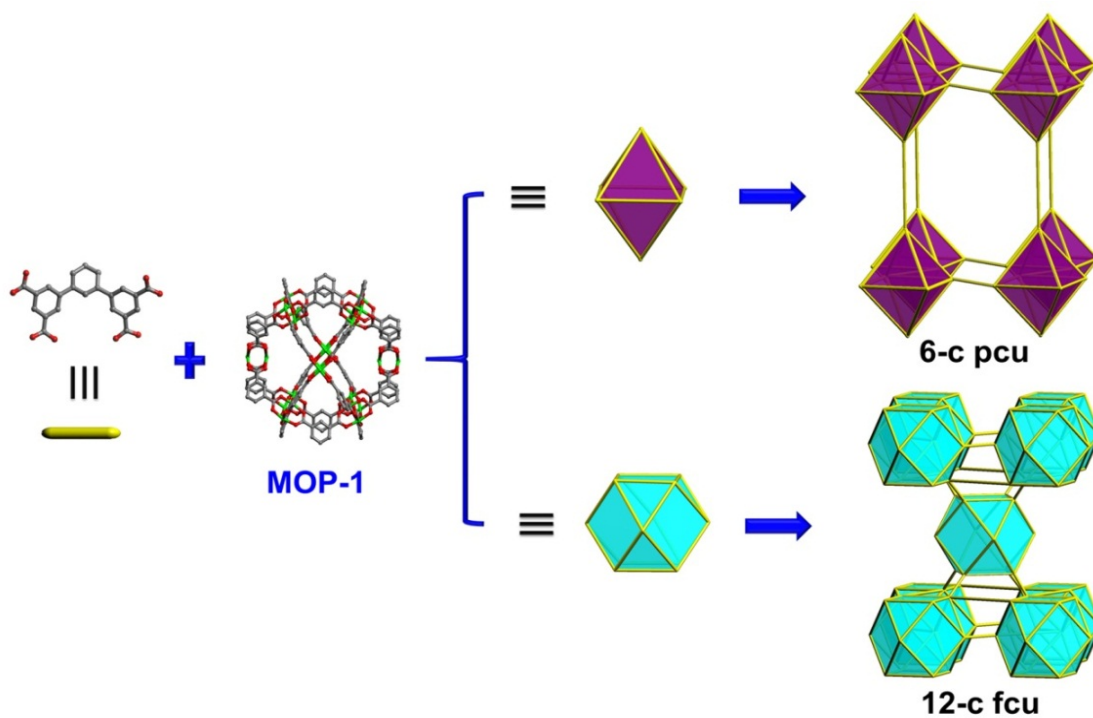


Fig. S4 The tpta⁴⁻ ligand is regarded as 2-c linker, and the MOP-1 can be viewed as an SBB

give rise to different topologies depending on the chosen vertices.

Stability Analysis

The stability analyses of JLU-Liu22 are shown in Fig. S5-S7, it indicates that **JLU-Liu22** exhibits good thermal stability. The powder XRD pattern for **JLU-Liu22** after adsorption-desorption tests is also in good agreement with the simulated one, indicating the stability of the material (Fig. S5). And the powder XRD patterns of temperature-dependent and different solvent exchanged samples are similar to the one simulated from the single-crystal structure, which proved the stability of the structure (Fig. S6-7).

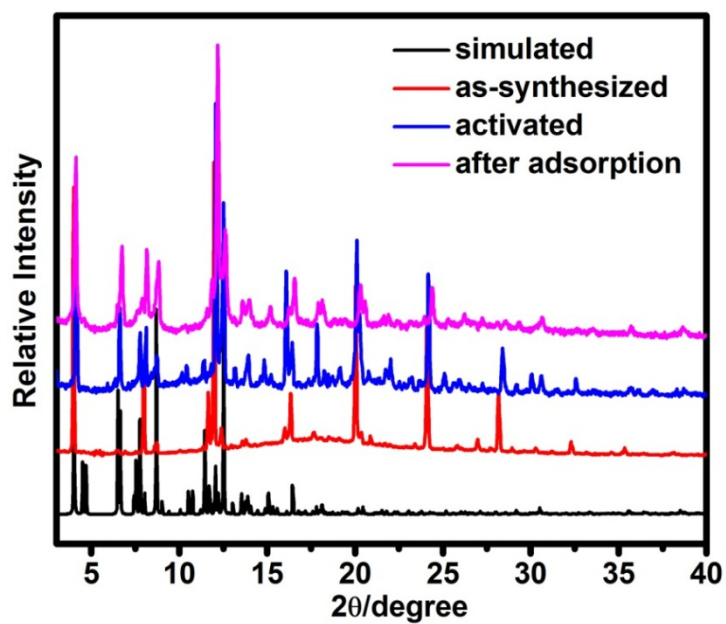


Fig. S5 Simulated, as-synthesized and activated powder X-ray diffraction (PXRD) patterns for JLU-Liu22 samples.

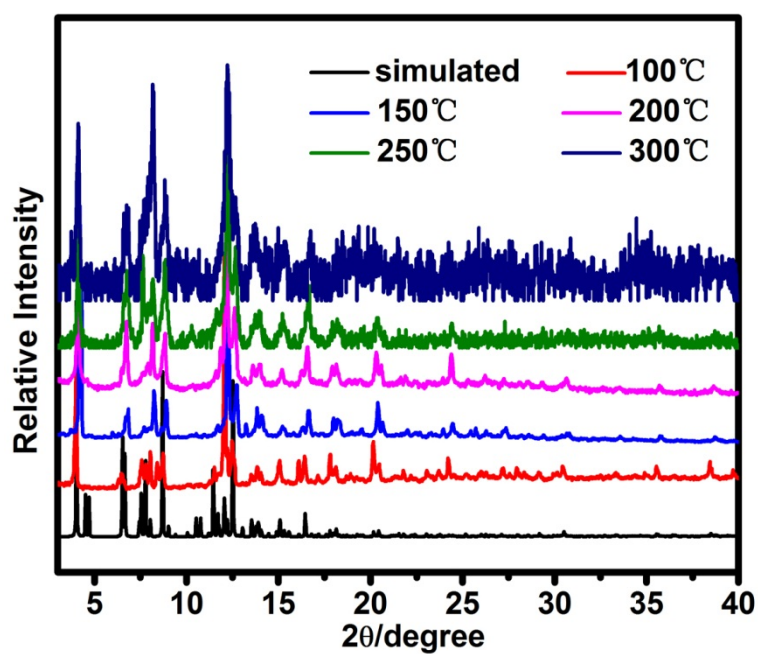


Fig. S6 The simulated and temperature-dependent powder XRD for JLU-Liu22 samples.

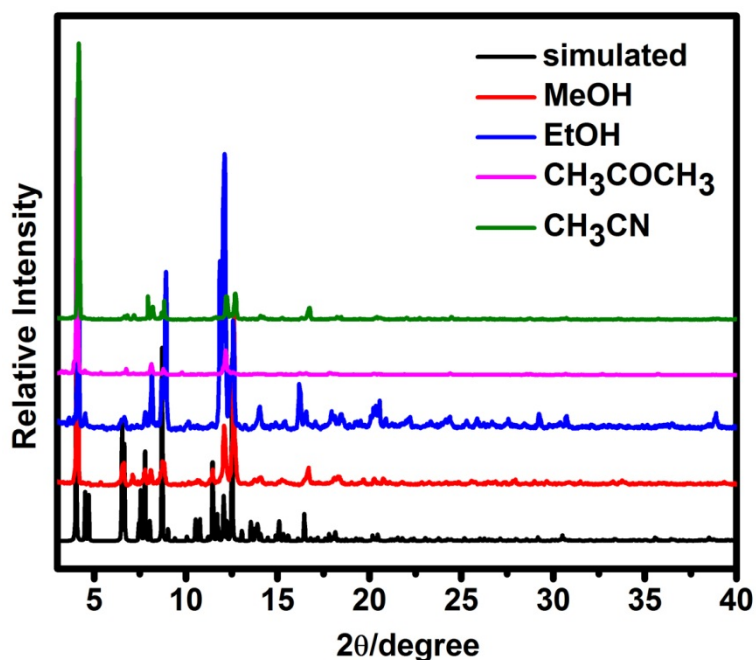


Fig. S7 The simulated and different solvent exchanged (MeOH, EtOH, CH₃COCH₃ and CH₃CN) powder XRD for **JLU-Liu22** samples.

Thermogravimetric Analysis

Thermogravimetric analysis (TGA) for **JLU-Liu22** shows a weight loss of 7.8 % between 35 and 105 °C, which corresponding to the loss of H₃O⁺ and guest H₂O molecules (calcd: 8.3 %). The second weight loss of 34.6 % that occurs between 105 and 300 °C should be attributed to the loss of guest DMA molecules and coordinated DMA molecules (calcd 33.8 %). Upon further heating, a weight loss of 40.2% should correspond to the release of the organic tpta⁴⁻ ligand and the coordinated COO⁻, and then the collapse of the framework (calcd 40.8 %) (Fig. S8).

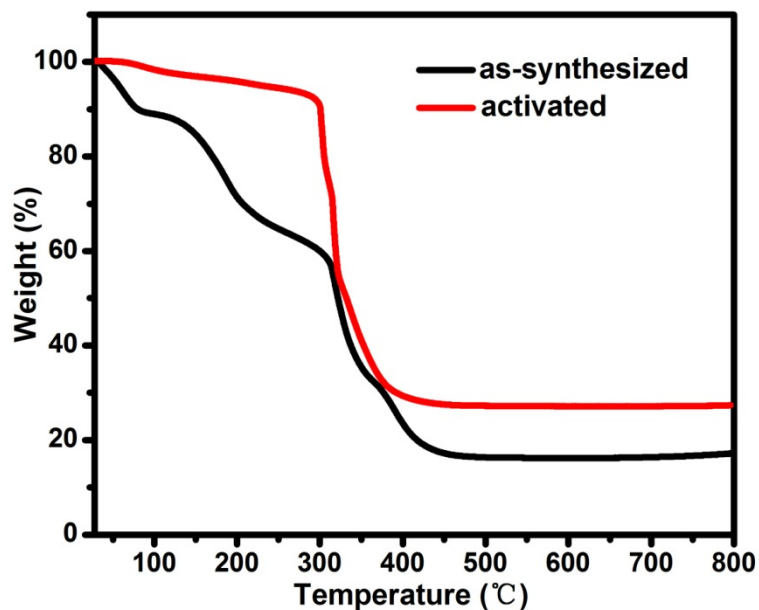


Fig. S8 Thermogravimetric analysis curves for the as-synthesized and activated samples of JLU-Liu22.

Gas sorption measurements

The N_2 , CO_2 , CH_4 , C_2H_6 and C_3H_8 gas adsorption measurements were performed on a Micromeritics ASAP 2420 and a Micromeritics ASAP 2020 instrument. Before gas adsorption measurements, the samples were degassed under a dynamic vacuum at 100 °C for 10 hours after solvent exchange with ethanol for 5 days to completely remove the non-volatile solvent molecules. A colour changed from bright-blue to deep purple-blue is a typical feature for Cu paddlewheel to generate open Cu sites. Moreover, it can be proved by TGA analysis (Fig. S8). The XRD pattern of activated sample is similar to the one simulated from the single-crystal structure, which further supported the sustained porosity (Fig. S5).

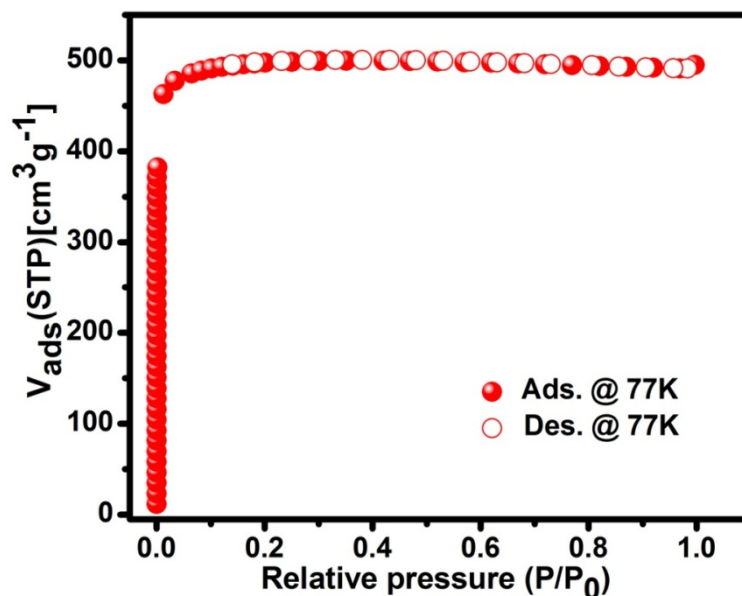


Fig. S9 Nitrogen sorption isotherms on JLU-Liu22 at 77 K. Adsorption: closed symbols; desorption: open symbols, respectively.

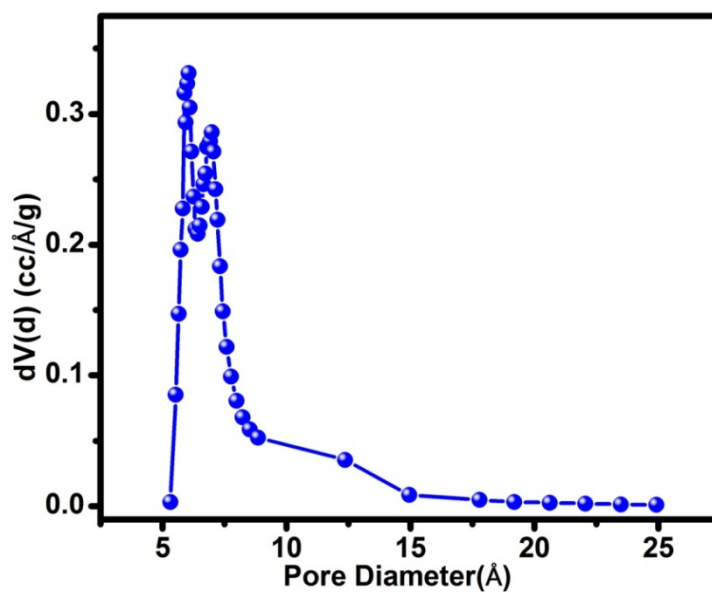


Fig. S10 The pore size distribution calculated using the DFT method.

Calculations of the Isothermic Heats of Gas Adsorption (Q_{st}):

The calculations of the isothermic heats (Q_{st}) of CO_2 , CH_4 , C_2H_6 and C_3H_8 gas adsorption are shown in Fig. S11-18. The results show that the Q_{st} values in Fig. S12 and Fig. S16 declines with the amount of adsorbate uptake. But in Fig. S14 and Fig. S18, Q_{st} values are found to increase with the amount of adsorbate uptake. To our knowledge, Q_{st} value increasing with the amount of adsorbate uptake is special and indeed exists. In 2013, Chen *et al.* reported a

similar phenomenon that the Q_{st} of CH_4 adsorption increase with the CH_4 loading, which can be attributed to both the open metal sites and suitable pore/cage sizes enable their moderately strong interaction with methane molecules.⁵ And this phenomenon also occurs for other gas molecules.⁶

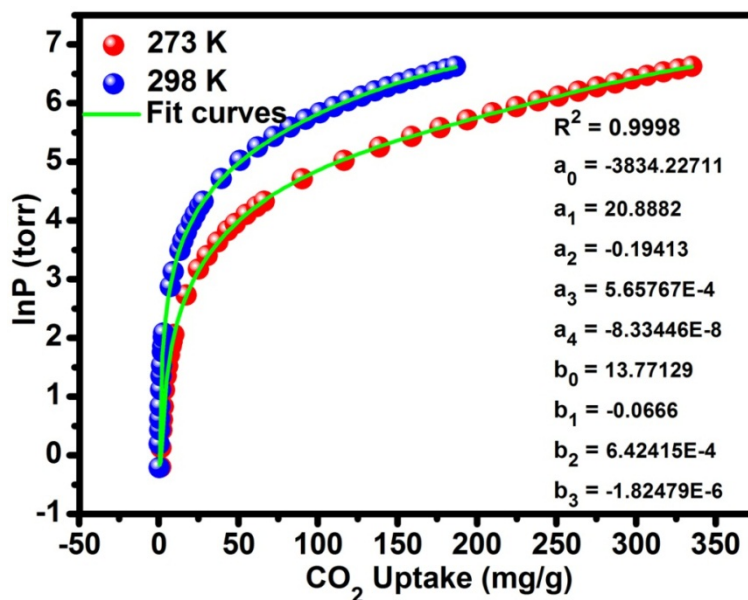


Fig. S11 Nonlinear curves fitting of CO_2 for JLU-Liu22 at 273 K and 298 K under 1 bar.

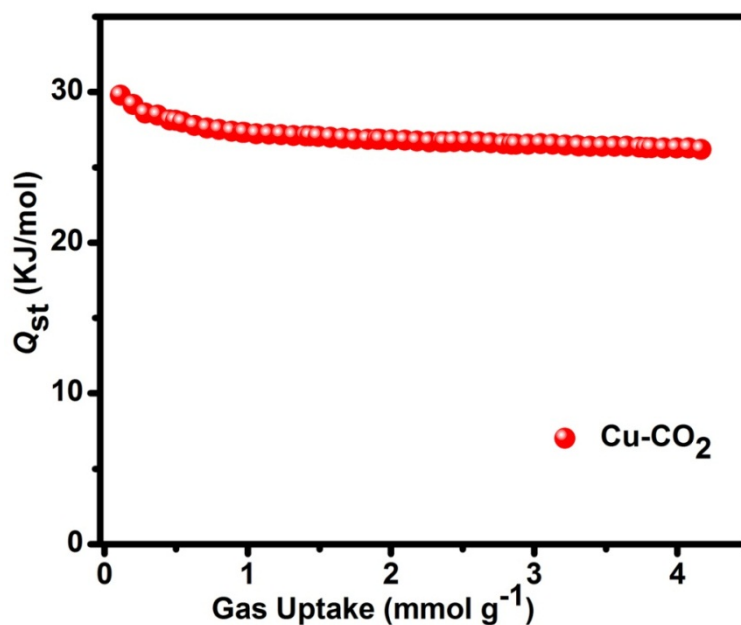


Fig. S12 Isothermic heat of CO_2 for JLU-Liu22.

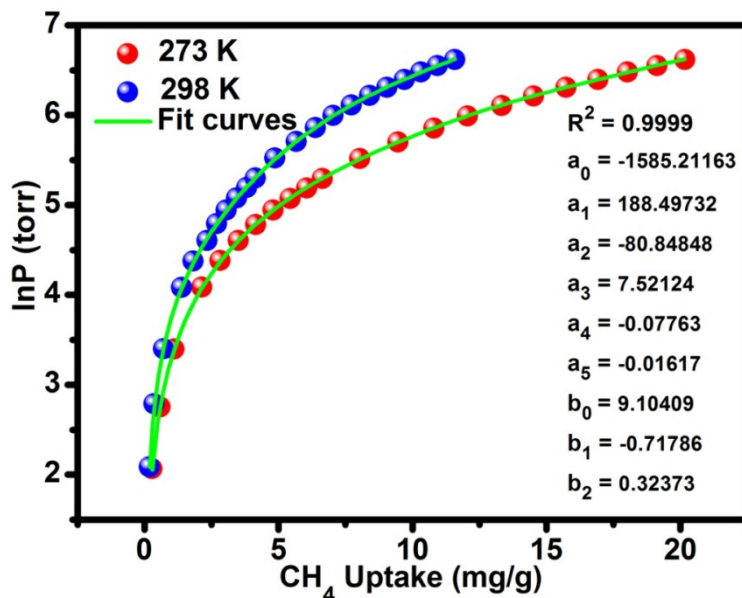


Fig. S13 Nonlinear curves fitting of CH₄ for JLU-Liu22 at 273 K and 298 K under 1 bar.

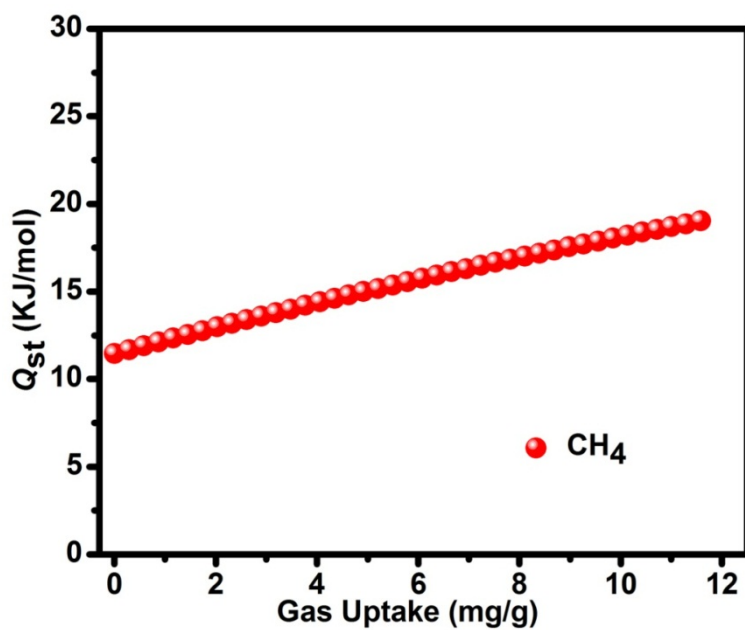


Fig. S14 Isosteric heat of CH₄ for JLU-Liu22.

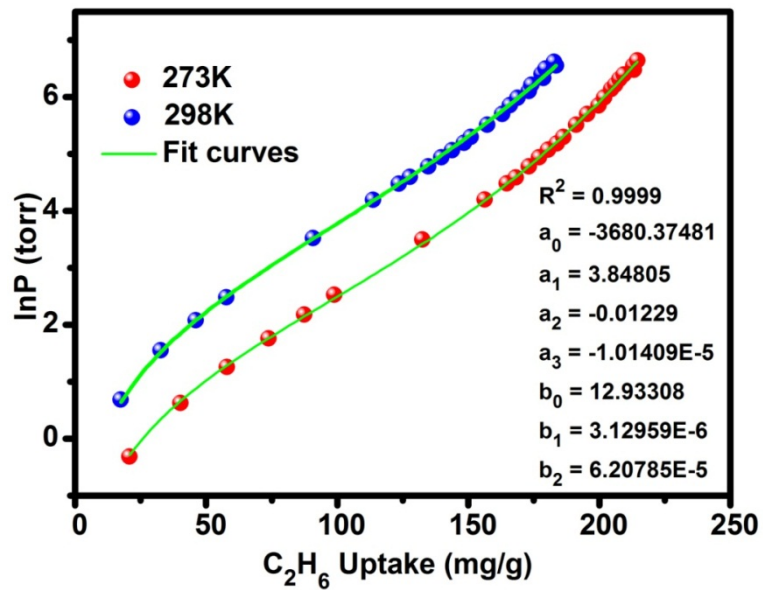


Fig. S15 Nonlinear curves fitting of C_2H_6 for JLU-Liu22 at 273 K and 298 K under 1 bar.

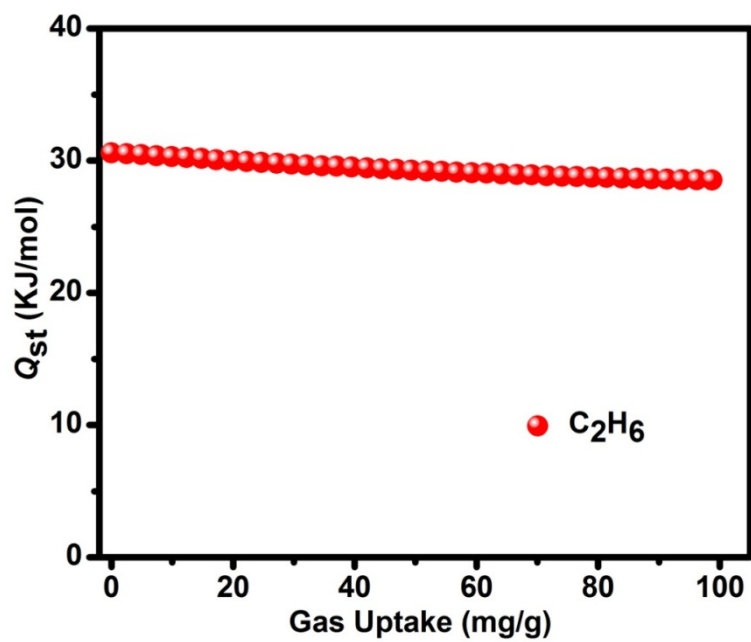


Fig. S16 Isosteric heat of C_2H_6 for JLU-Liu22.

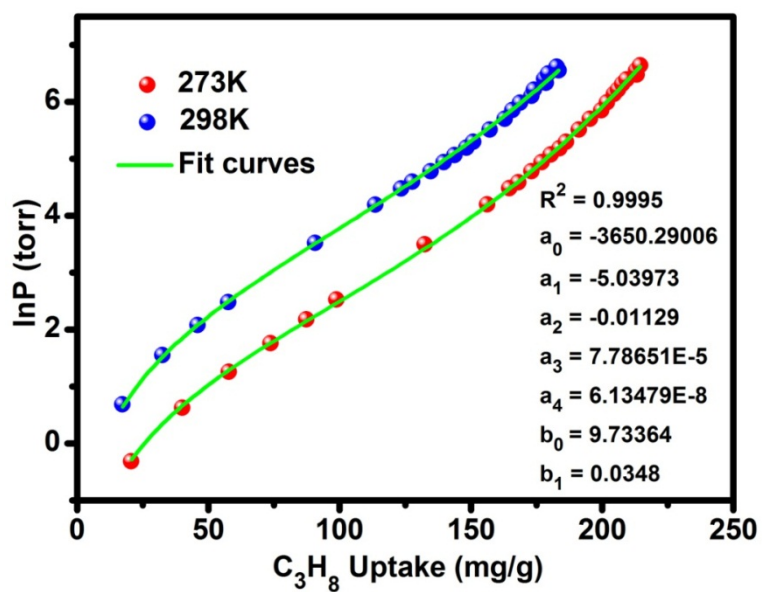


Fig. S17 Nonlinear curves fitting of C_3H_8 for JLU-Liu22 at 273 K and 298 K under 1 bar.

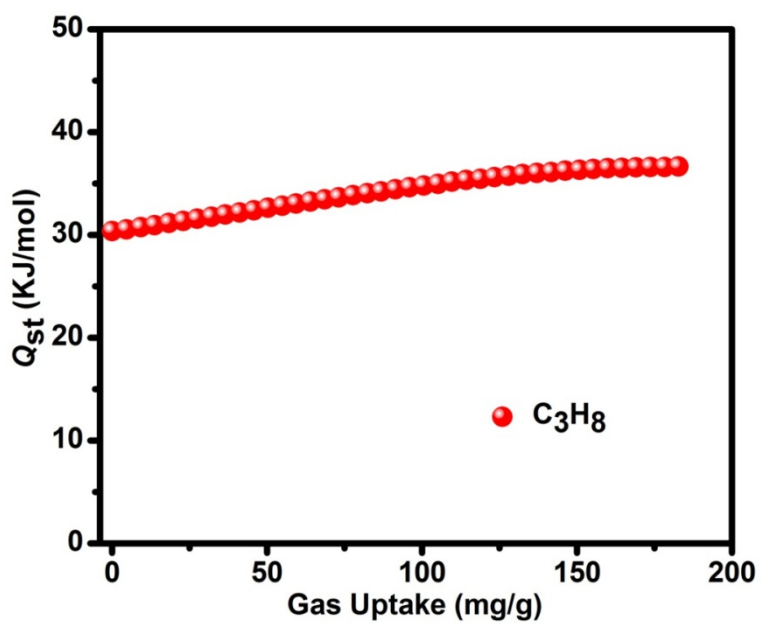


Fig. S18 Isosteric heat of C_3H_8 for JLU-Liu22.

Table 1. Comparison of CO₂ uptake capacities for MOFs based on the ligands similar to H₄tpta ligand under 1 bar.

MOFs	S_{BET} [m ² g ⁻¹]	CO ₂ Capacity [wt %]	Q_{st} [KJ mol ⁻¹]	T [K]	Ref.
JLU-Liu22 ^a	1487	33.4	30	273	This work
PCN-306 (H) ^a	1927	22.9	24	273	7
PCN-305 (N) ^b	1720	23.2	24	273	7
PCN-307 (CH ₃) ^c	1376	23.2	23	273	7
PCN-308 (CF ₃) ^d	1418	24.8	22	273	7
JLU-Liu5 ^e	707	20.0	34.6	273	8
JLU-Liu6 ^e	544	13.7	35.8	273	8
PCN-88 ^f	3308	31.4	27	273	9
NTU-111 ^g	2450	24.5	30.7	273	10
NTU-101-Cu ^g	2017	16.6	25	273	11
PCN-124 ^h	1372	28.6	26.3	273	12
[Cu ₂₄ (L) ₁₂ (H ₂ O) ₁₂] 2DMF 180H ₂ O ⁱ	1879	12.5	N. A.	298	13

a)-i) Ligands are corresponding with the above compounds. N. A.: Not Available. The article do not list the data.

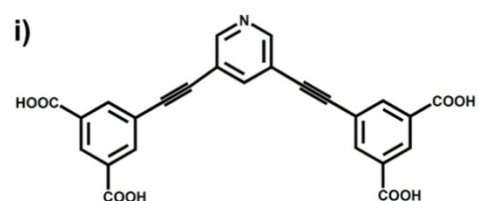
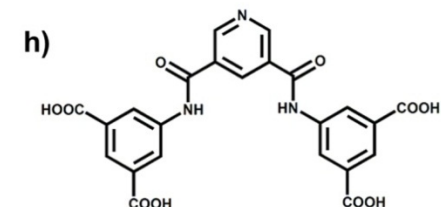
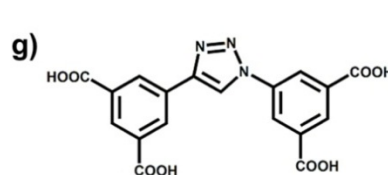
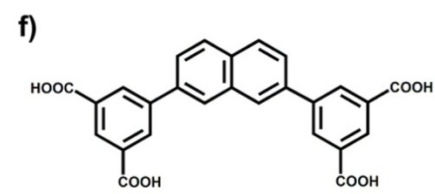
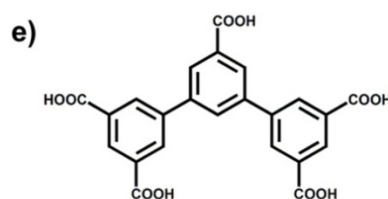
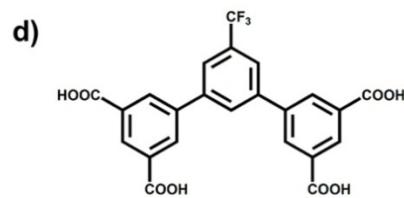
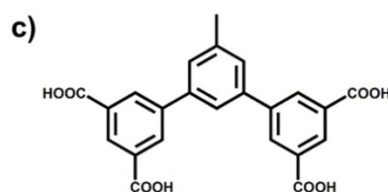
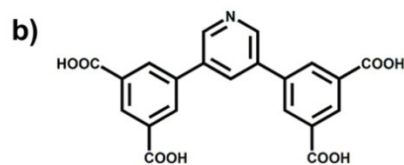
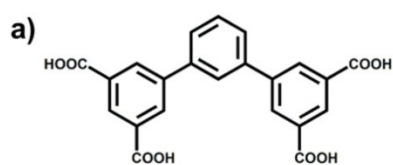


Table S2. Crystal data and structure refinement for **JLU-Liu22**.

Compound	JLU-Liu22
Empirical formula	C ₁₁₁ H ₁₅₆ Cu ₆ N ₁₁ O ₅₀
Formula weight	2825.70
Temperature (K)	293(2)
Wavelength (Å)	0.71073
Crystal system	Tetragonal
Space group	<i>P4/mnc</i>
<i>a</i> (Å)	26.582(4)
<i>b</i> (Å)	26.582(4)
<i>c</i> (Å)	39.190(8)
α (deg)	90
β (deg)	90
γ (deg)	90
Volume (Å ³)	27692(10)
Z, Dcalc (Mg/m ³)	8, 1.356
Absorption coefficient (mm ⁻¹)	0.991
F(000)	11784
Crystal size (mm)	0.27 × 0.23 × 0.19
Theta range for data collection	0.926 to 25.055
Goodness-of-fit on <i>F</i> ²	1.024
Final R indices [<i>I</i> > 2σ(<i>I</i>)]	<i>R</i> ₁ = 0.0385, <i>wR</i> ₂ = 0.1038
R indices (all data)	<i>R</i> ₁ = 0.0558, <i>wR</i> ₂ = 0.1088

$$R_1 = \frac{\sum ||F_o| - |F_c||}{\sum |F_o|}, wR_2 = \left[\frac{\sum [w(F_o^2 - F_c^2)^2]}{\sum [w(F_o^2)^2]} \right]^{1/2}$$

Table S3. Selected bond lengths [\AA] and angles [$^\circ$] for **JLU-Liu22**.

Cu(1)-O(9)	1.9349(17)	Cu(1)-O(1)	1.9515(18)	Cu(3)-O(15)	2.137(3)
Cu(1)-O(7)#1	1.9693(18)	Cu(1)-O(3)#2	1.9707(19)	Cu(3)-Cu(4)	2.6468(7)
Cu(1)-O(13)	2.146(2)	Cu(1)-Cu(2)	2.6486(5)	Cu(4)-O(6)	1.9527(19)
Cu(2)-O(4)#2	1.9588(18)	Cu(2)-O(8)#1	1.9633(17)	Cu(4)-O(6)#3	1.9528(19)
Cu(2)-O(2)	1.9672(17)	Cu(2)-O(10)	1.9860(17)	Cu(4)-O(12)#4	1.9561(19)
Cu(2)-O(14)	2.059(2)	Cu(3)-O(5)#3	1.9617(19)	Cu(4)-O(12)#5	1.9561(19)
Cu(3)-O(5)	1.9618(19)	Cu(3)-O(11)#4	1.9726(18)	Cu(4)-O(16)	2.165(3)
Cu(3)-O(11)#5	1.9726(18)				
O(9)-Cu(1)-O(1)	171.45(8)	O(9)-Cu(1)-O(7)#1	90.36(8)	O(1)-Cu(1)-O(7)#1	89.45(9)
O(9)-Cu(1)-O(3)#2	88.57(9)	O(1)-Cu(1)-O(3)#2	89.36(9)	O(7)#1-Cu(1)-O(3)#2	164.71(8)
O(1)-Cu(1)-O(13)	96.30(9)	O(9)-Cu(1)-O(13)	92.23(10)	O(7)#1-Cu(1)-O(13)	95.05(10)
O(3)#2-Cu(1)-O(13)	100.22(10)	O(4)#2-Cu(2)-O(8)#1	170.88(8)	O(4)#2-Cu(2)-O(2)	88.07(8)
O(8)#1-Cu(2)-O(2)	89.14(8)	O(4)#2-Cu(2)-O(10)	88.51(8)	O(8)#1-Cu(2)-O(10)	91.76(8)
O(2)-Cu(2)-O(10)	163.72(8)	O(4)#2-Cu(2)-O(14)	91.83(9)	O(8)#1-Cu(2)-O(14)	97.27(9)
O(2)-Cu(2)-O(14)	103.71(9)	O(10)-Cu(2)-O(14)	92.30(9)	O(5)#3-Cu(3)-O(5)	91.46(12)
O(5)#3-Cu(3)-O(11)#4	87.35(9)	O(5)-Cu(3)-O(11)#4	167.78(8)	O(5)#3-Cu(3)-O(11)#5	167.78(8)
O(5)-Cu(3)-O(11)#5	87.35(9)	O(11)#4-Cu(3)-O(11)#5	91.23(12)	O(5)#3-Cu(3)-O(15)	95.62(10)
O(5)-Cu(3)-O(15)	95.62(10)	O(11)#4-Cu(3)-O(15)	96.60(10)	O(11)#5-Cu(3)-O(15)	96.60(10)
O(6)-Cu(4)-O(6)#3	91.07(13)	O(6)-Cu(4)-O(12)#4	168.13(8)	O(6)#3-Cu(4)-O(12)#4	87.46(9)
O(6)-Cu(4)-O(12)#5	87.46(9)	O(6)#3-Cu(4)-O(12)#5	168.13(8)	O(6)#3-Cu(4)-O(12)#5	168.13(8)
O(12)#4-Cu(4)-O(12)#5	91.57(13)	O(6)-Cu(4)-O(16)	96.27(9)	O(6)#3-Cu(4)-O(16)	96.27(9)
O(12)#4-Cu(4)-O(16)	95.59(9)	O(12)#5-Cu(4)-O(16)	95.59(9)		

Symmetry transformations used to generate equivalent atoms:

#1 -y+1/2,-x+1/2,-z+1/2 #2 -y,x,z #3 x,y,-z+1 #4 x+1/2,-y+1/2,z+1/2

#5 x+1/2,-y+1/2,-z+1/2 #6 y,-x,z #7 x-1/2,-y+1/2,z-1/2 #8 -x,-y+1,z

Table S4 The refined parameters for the Dual-site Langmuir-Freundlich equations fit for the pure isotherms of CO₂, CH₄, C₂H₆ and C₃H₈ for **JLU-Liu22** at 298 K.

adsorbate	q_{m1} [mmol g ⁻¹]	b_1 [kPa ⁻¹]	n_1	q_{m2} [mmol g ⁻¹]	b_2 [kPa ⁻¹]	n_2	R^2
CO ₂	0.48766	0.08391	1.00430	13.07611	0.00255	1.10165	0.9999
CH ₄	2.0182	8.412E-5	1.69979	0.48596	0.02067	1.10828	0.9999
C ₂ H ₆	7.46154	0.0100	0.77692	0.04238	0.03074	1.09307	0.9999
C ₃ H ₈	1.36163	0.90161	1.00000	3.38856	0.11903	0.80558	0.9997

Reference

1. A. L. Myers, J. M. Prausnitz, *AIChE J.* 1965, **11**, 121-127.
2. J. L. C. Rowsell, O. M. Yaghi, *J. Am. Chem. Soc.*, 2006, **128**, 1304-1315.
3. Sheldrick, G. M. SHELXTL-NT, version 5.1; Bruker AXS Inc., Madison, WI, 1997.
4. V. A. Blatov, A. P. Shevchenko, D. M. Proserpio, *Cryst. Growth Des.*, 2014, **14**, 3576-3683.
5. X. Rao, J. Cai, J. Yu, Y. He, C. Wu, W. Zhou, T. Yildirim, B. Chen and G. Qian, *Chem.*

- Commun.*, 2013, **49**, 6719-6721.
6. (a) P. Nugent, Y. Belmabkhout, S. D. Burd, A. J. Cairns, R. Luebke, K. Forrest, T. Pham, S. Ma, B. Space, L. Wojtas, M. Eddaoudi and M. J. Zaworotko, *Nature* 2013, **495**, 80-84; (b) P. S. Nugent, V. L. Rhodus, T. Pham, K. Forrest, L. Wojtas, B. Space and M. J. Zaworotko, *J. Am. Chem. Soc.*, 2013, **135**, 10950-10953; (c) J. Cai, X. Rao, Y. He, J. Yu, C. Wu, W. Zhou, T. Yildirim, B. Chen and G. Qian, *Chem. Commun.*, 2014, **50**, 1552-1554; (d) S. Meng, H. Ma, L. Jiang, H. Ren and G. Zhu, *J. Mater. Chem. A*, 2014, **2**, 14536-14541; (e) S. Yao, D. Wang, Y. Cao, G. Li, Q. Huo and Y. Liu, *J. Mater. Chem. A.*, 2015, **3**, 16627-16632.
 7. Y. Liu, J.-R. Li, W. M. Verdegaal, T.-F. Liu and H.-C. Zhou, *Chem. Eur. J.*, 2013, **19**, 5637-5643.
 8. D. Wang, T. Zhao, Y. Cao, S. Yao, G. Li, Q. Huo and Y. Liu, *Chem. Commun.*, 2014, **50**, 8648-8650.
 9. J.-R. Li, J. Yu, W. Lu, L.-B. Sun, J. Sculley, P. B. Balbuena and H.-C. Zhou, *Nat Commun.*, 2013, **4**, 1538-1545.
 10. P.-Z. Li, X.-J. Wang, K. Zhang, A. Nalaparaju, R. Zou, R. Zou, J. Jiang and Y. Zhao, *Chem. Commun.*, 2014, **50**, 4683-4685.
 11. X.-J. Wang, P.-Z. Li, L. Liu, Q. Zhang, P. Borah, J. D. Wong, X. X. Chan, G. Rakesh, Y. Li and Y. Zhao, *Chem. Commun.*, 2012, **48**, 10286-10288.
 12. J. Park, J.-R. Li, Y.-P. Chen, J. Yu, A. A. Yakovenko, Z. U. Wang, L.-B. Sun, P. B. Balbuena and H.-C. Zhou, *Chem. Commun.*, 2012, **48**, 9995-9997.
 13. P. Zhang, B. Li, Y. Zhao, X. Meng and T. Zhang, *Chem. Commun.*, 2011, **47**, 7722-7724.